# SANDIA REPORT

# Enhanced Molecular Dynamics for Simulating Porous Interphase Layers in Batteries

Jeremy A. Templeton, Reese E. Jones, Jonathan Lee, Bryan M. Wong, Jonathan A. Zimmerman

Sandia National Laboratories

Issued by Sandia National Laboratories, operated for the United States Department of Energy by Sandia Corporation.

# Enhanced Molecular Dynamics for Simulating Porous Interphase Layers in Batteries

Jeremy A. Templeton, Reese E. Jones,
Bryan M. Wong, Jonathan A. Zimmerman
Sandia National Laboratories, P.O. Box 969
Livermore, CA 94550-0969

Jonathan Lee
Rice University, PO Box 1892
Houston TX 77251-1892

**Abstract**

Understanding charge transport processes at a molecular level using computational techniques is currently hindered by a lack of appropriate models for incorporating anistropic electric fields in molecular dynamics (MD) simulations. An important technological example is ion transport through solid-electrolyte interphase (SEI) layers that form in many common types of batteries. These layers regulate the rate at which electro-chemical reactions occur, affecting power, safety, and reliability. In this work, we develop a model for incorporating electric fields in MD using an atomistic-to-continuum framework. This framework provides the mathematical and algorithmic infrastructure to couple finite element (FE) representations of continuous data with atomic data. In this application, the electric potential is represented on a FE mesh and is calculated from a Poisson equation with source terms determined by the distribution of the atomic charges. Boundary conditions can be imposed naturally using the FE description of the potential, which then propagates to each atom through modified forces. The method is verified using simulations where analytical or theoretical solutions are known. Calculations of salt water solutions in complex domains are performed to understand how ions are attracted to charged surfaces in the presence of electric fields and interfering media.

# Acknowledgment

# Contents

# Appendix

# List of Figures

# Chapter 1

# Introduction

The reliance of the United States economy on fossil fuels has led to significant national security concerns regarding the impact of $CO_2$ emissions on the global climate and domestic dependence on foreign petroleum sources. Mitigation of these threats will require a fundamental shift in how our society harvests, stores, and uses energy. One of the most important technologies that will likely play a significant role in this transformation is electrical energy storage using batteries. Key impact areas for batteries include energy storage for transportation to reduce dependence on fossil fuels and as capacitors to regulate the intermittent power generated by renewable sources. Unfortunately, battery technology must make significant advances in the next decade if it is contribute to the nation's energy solutions.

Detracting from the potential of batteries to offer an energy storage solution for personal transportation are their lower energy density, lower power output, longer recharge time, and reduced safety as compared to conventional internal combustion engines. Several centuries of investigation have not changed the basic operating principles of batteries. Improving their technological basis such that they can contribute to energy solutions will require significant enhancements to our ability to understand and engineer charge transport processes at the nanoscale, as discussed in the DOE Basic Energy Sciences (BES) report on research needs in electrical energy storage devices (EESDs) [4]. While many different improvements are needed, an important area is enhanced capacity to develop computational models of battery behavior at the molecular level.

Molecular dynamics (MD) simulations for understanding complex processes at the atomic scale have seen a radical improvement in the past three decades. At present, however, most MD simulations are still performed in periodic domains due to the difficulty of accurately prescribing boundary conditions that break the spatial symmetries and enable many problems of scientific interest to be examined. An important example is the solid-electrolyte interphase (SEI) layer, which forms on the anode in many common types of EESDs, such as lithium-ion batteries. It is a collection of different solid phases formed on the electrode from the solvent and solute species. The layer is both beneficial and detrimental, as it protects the anode but its porous structure limits the rate at which ions can move from the bulk electrolyte to the electrode. Understanding this layer's dynamics, with the goal of deliberately engineered SEI layers, is a necessary step to enable next generation battery technologies.

The BES report points to the inability to represent inhomogeneous electric fields within MD as one of the most important barriers to MD playing a role in modeling the SEI layer.

7

This statement is a direct consequence of the aforementioned difficulty in breaking spatial symmetry in MD simulations. By examining the current methods for incorporating long-range electric field effects in MD, the limitation can be better understood. The two most common approaches are Ewald summations and the particle-particle/particle-mesh (PPPM) method [6]. Both use the following decomposition of the electric potential due to point charges:

$$U = \frac{1}{2} \sum_{\alpha \in \mathcal{A}} \sum_{\substack{\beta \in \mathcal{A} \\ \beta \neq \alpha}} \left( \frac{c^\alpha c^\beta}{r_{\alpha\beta}} - \int \int \frac{\rho^\alpha(r)\rho^\beta(r')}{|r - r'|} \, dr \, dr' \right)$$

$$+ \frac{1}{2} \sum_{\alpha \in \mathcal{A}} \sum_{\beta \in \mathcal{A}} \int \int \frac{\rho^\alpha(r)\rho^\beta(r')}{|r - r'|} \, dr \, dr' - \frac{1}{2} \sum_{\alpha \in \mathcal{A}} \int \int \frac{\rho^\alpha(r)\rho^\alpha(r')}{|r - r'|} \, dr \, dr'. \quad (1.1)$$

The first term accounts for short-range interactions between particles while the remaining terms describe the long-range effects of a smooth charge distribution, $\rho$. In both methods, $\rho$ is represented using a Gaussian distribution. Ewald sums analytically solve this equation using the Fourier space representation of the convolution of each atom's associated $\rho$. The PPPM method instead restricts $\rho$ to a grid and then computes its Fourier transform to determine the total electrostatic potential. Of the two, PPPM is more widely used, particularly for large systems [12].

Despite the differences in performance that drive the preference of one method over the other, both require analysis in Fourier space to solve eq. (1.1), and are thus are only applicable in periodic domains. Further, there is no mechanism within the methods to assign the typical boundary conditions associated with continuous potential fields. To overcome this deficiency, the present work develops a new electric field model within the atomistic-to-continuum (AtC) framework [17, 7, 21] currently implemented in the MD code LAMMPS (see [11] and http://lammps.sandia.gov). AtC methods involve coupling the discrete atomic dynamics in MD to continuous processes represented by finite elements (FE). For this application, the FE will track the long-range electric field while the MD calculates the atomic motion. The remainder of this report describes the mathematical formulation of the model and presents some example calculations.

# Chapter 2

# Mathematical Formulation

## 2.1 Mathematical Framework for Multiscale Modeling

The multiscale modeling framework used in this work is based on AtC coupling as implemented in the MD code LAMMPS. It is based on approximate FE projections of MD data to restrict atomic quantities to an FE mesh and corresponding interpolation operators to compute FE quantities on atoms. For example, the FE projection, $\hat{\rho}(\mathbf{x})$, to a continuous density field, $\rho(\mathbf{x})$ is

$$\int \delta\hat{\rho}\,\hat{\rho}\,\mathrm{d}V = \int \delta\hat{\rho}\,\rho\,\mathrm{d}V, \tag{2.1}$$

$$\hat{\rho}(\mathbf{x}) = \sum_I \delta\hat{\rho}(\mathbf{x})\hat{\rho}, \tag{2.2}$$

which projects the continuous field onto a space spanned by a finite set of test functions. Typically, FE data takes the form of nodal densities (e.g., mass density and momentum density) while the atomic data are primitive kinematic variables (e.g., mass and velocity). These distinct quantities are related by defining atomic densities by a small but finite volume $\Delta V_\rho^\alpha$, to be determined later. In this work, it is assumed that the MD and FE domains exactly coincide on the domain $\Omega \subset \mathbb{R}^3$. Because continuous integration is not well defined over the discrete atomic locations, the projection of a continuous function onto its FE representation,

$$\sum_{J\in\mathcal{F}} \int_\Omega N_I N_J \rho_J \,\mathrm{d}V = \int_\Omega N_I \rho(\mathbf{x})\,\mathrm{d}V, \quad \forall I \in \mathcal{F}, \tag{2.3}$$

is approximated by the sums

$$\sum_{J\in\mathcal{F}}\sum_{\alpha\in\mathcal{A}} N_I^\alpha N_J^\alpha \rho_J \Delta V^\alpha = \sum_{\alpha\in\mathcal{A}} N_I^\alpha \frac{m^\alpha}{\Delta V_\rho^\alpha} \Delta V^\alpha, \quad \forall I \in \mathcal{F}, \tag{2.4}$$

using the approximation

$$\rho(\mathbf{x}^\alpha) \equiv \rho^\alpha = \frac{m^\alpha}{\Delta V_\rho^\alpha}. \tag{2.5}$$

In these equations, $N$ indicates the finite set of FE shape functions which have finite element indices in the set $\mathcal{F}$ (replacing the more general trial functions in eq. (2.1)), denoted

by subscript Roman letters. Superscript Greek letters denote atomic indices from the set $\mathcal{A}$ enumerating the atoms in the system, with $N_I^\alpha$ denoting the value of the shape function associated with node $I$ at the position of atom $\alpha$, $\mathbf{x}^\alpha$. The variables $\rho$ and $m$ denote density and mass, respectively. By equating the two atomic volumes $\Delta V_\rho^\alpha = \Delta V^\alpha$, the fundamental relationship between a continuous density and its associated atomic quantity is derived (with the set notation removed from the remainder for clarity except where needed):

$$\sum_J \sum_\alpha N_I^\alpha N_J^\alpha \rho_J \Delta V^\alpha = \sum_\alpha N_I^\alpha m^\alpha. \tag{2.6}$$

A common application of eq. (2.6) would be to consider quantities only in a subset of the atoms, $\mathcal{A}'$, for example to compute the density of a single species. In this case, the governing equation would be

$$\sum_J \sum_{\alpha \in \mathcal{A}} N_I^\alpha N_J^\alpha \rho_J \Delta V^\alpha = \sum_{\alpha' \in \mathcal{A}'} N_I^{\alpha'} m^{\alpha'}. \tag{2.7}$$

This is equivalent to to defining the mass of all atoms not in set $\mathcal{A}$ to be zero within the approximate quadrature of eq. (2.6). The atom sets are different on the right- and left-hand sides because the left-hand side represents approximate integration quadrature while the right-hand side is a weighted average over a set of atoms. Henceforth, the notation $\alpha'$ will denote sums taken over subsets of the set of all atoms.

The present work considers all quantities to be computed in the Eulerian frame. Therefore, both $N_I^\alpha$ and $\Delta V^\alpha$ will vary with time as atoms move through space. The associated atomic volumes change with time because eq. (2.6) is a statement about shape function-averaged mass per node, so a constant volume would not correctly assign mass to the node. This observation implies the atomic volumes should be related to both the set of shape functions and set of atoms present in the system. Therefore, consider the postulate that a nodal atomic volume variable exits, $\Delta V_I$, and it is used to compute the atomic volume using FE interpolation:

$$\Delta V(\mathbf{x}^\alpha) \equiv \Delta V^\alpha = \sum_I N_I^\alpha \Delta V_I. \tag{2.8}$$

To be a rational choice for the atomic volume, eq. (2.4) must be an accurate approximation of eq. (2.3). More generally, a function that satisfied the family of consistency conditions

$$\sum_\alpha N_I^\alpha \Delta V^\alpha = \int_\Omega N_I \, dV,$$

$$\sum_\alpha N_I^\alpha N_J^\alpha \Delta V^\alpha = \int_\Omega N_I N_J \, dV, \tag{2.9}$$

$$\sum_\alpha N_I^\alpha N_J^\alpha N_K^\alpha \Delta V^\alpha = \int_\Omega N_I N_J N_K \, dV,$$

$$\vdots$$

would guarantee that all integrals involving FE shape functions matched their discrete approximations. However, this is an infinite set of constraints, so instead only the $m = 1$

constraint is used because it results in a well-posed system of equations for $\Delta V_I$. By substituting eq. (2.8) into the first constraint of eq. (2.9), the equation governing the nodal atomic volumes is

$$\sum_\alpha N_I^\alpha \sum_J N_J^\alpha \Delta V_J = \int_\Omega N_I \, \mathrm{d}V. \tag{2.10}$$

The mathematical structure of this formulation can be related to the standard notion of continuum models of fluid flow by taking the time derivative of eq. (2.6). On the right-hand side, the result is

$$\frac{\mathrm{d}}{\mathrm{d}t} \sum_\alpha N_I^\alpha \, m^\alpha = \sum_\alpha m^\alpha \frac{\mathrm{d}}{\mathrm{d}t} N_I^\alpha = \sum_\alpha m^\alpha \nabla N_I^\alpha \cdot \mathbf{v}^\alpha. \tag{2.11}$$

The time derivative of the left-hand side produces two terms:

$$\frac{\mathrm{d}}{\mathrm{d}t}\left[\sum_\alpha \sum_J N_I^\alpha N_J^\alpha \rho_J \Delta V^\alpha\right] = \sum_J \sum_\alpha \left[(N_I^\alpha N_J^\alpha \Delta V^\alpha)\frac{\mathrm{d}\rho_J}{\mathrm{d}t} + \frac{\mathrm{d}}{\mathrm{d}t}(N_I^\alpha N_J^\alpha \Delta V^\alpha)\rho_J\right]. \tag{2.12}$$

For the left-hand side, the important relationship is

$$\sum_\alpha N_I^\alpha N_J^\alpha \Delta V^\alpha \approx \int_\Omega N_I N_J \, \mathrm{d}V. \tag{2.13}$$

This is not exact because only one of the constraints in eq. (2.9) can be satisfied, and it is eq. (2.10) corresponding to the first moment rather than the second moment. If this approximation is exact, then the term multiplying $\mathrm{d}\rho_J/\mathrm{d}t$ is the standard FE mass matrix while

$$\frac{\mathrm{d}}{\mathrm{d}t}\left(\int_\Omega N_I N_J \, \mathrm{d}V\right) = 0. \tag{2.14}$$

To get eq. (2.11) into the appropriate form, consider

$$\sum_\alpha m^\alpha \nabla N_I^\alpha \cdot \mathbf{v}^\alpha = \sum_\alpha \nabla N_I^\alpha \cdot (\rho^\alpha \mathbf{v}^\alpha)\,\Delta V^\alpha$$

$$\approx \int_\Omega \nabla N_I \cdot (\rho \mathbf{v}) \, \mathrm{d}V$$

$$= \int_{\partial\Omega} N_I\,(\rho\mathbf{v}) \cdot \mathbf{n} \, \mathrm{d}S - \int_\Omega N_I \nabla \cdot (\rho\mathbf{v}) \, \mathrm{d}V.$$

The accuracy of this equation is a function only of the approximate MD quadrature.

The standard, continuous time evolution equation is

$$\frac{\mathrm{d}\rho}{\mathrm{d}t} + \nabla \cdot (\rho\mathbf{v}) = 0, \tag{2.15}$$

which has the usual FE approximation:

$$\sum_J \int_\Omega N_I N_J \frac{\mathrm{d}\rho_I}{\mathrm{d}t} \, \mathrm{d}V = \int_\Omega N_I \nabla \cdot (\rho\mathbf{v}) \, \mathrm{d}V = \int_{\partial\Omega} N_I\,(\rho\mathbf{v}) \cdot \mathbf{n} \, \mathrm{d}S - \int_\Omega N_I \nabla \cdot (\rho\mathbf{v}) \, \mathrm{d}V. \tag{2.16}$$

Hence, if the atomic quadrature is exact, then the standard FE approximation to the mass conservation equation is obtained. The precision of the quadrature is related to the number of atoms in each element, so as the ratio of atoms per element becomes large, the correct continuous transport equation is recovered.

## 2.2   Electric Field Model

### 2.2.1   Long-Range Electric Field

The emphasis of this work is on the formulation of an AtC electric field in which long-range interactions are computed on a FE mesh and communicated to the atoms, while short-range interactions are modeled directly by Coulombic interactions to maintain high fidelity. Each charged atom contributes to the electric potential, and because the potential is long-range, a direct restriction of the electric potential would be prohibitively costly, just as direct computation of the long-range Coulombic interactions is costly. Instead, the equation governing the electric potential will be solved on the FE mesh. The continuous equation governing the electric potential is

$$\nabla^2 \phi = -\frac{1}{\epsilon_0} q, \tag{2.17}$$

with $q$ being the charge density and $\epsilon_0$ the dielectric constant. The charge density of atom $\alpha$ can be written as

$$q^\alpha = \frac{c^\alpha}{\Delta V^\alpha}, \tag{2.18}$$

where $c^\alpha$ is the charge of atom $\alpha$. Using the fundamental AtC projection, eq. (2.6), the relationship between the two charge descriptions is

$$\sum_{\alpha \in \mathcal{A}} N_I^\alpha \sum_J N_J^\alpha q_J \, \Delta V^\alpha = \sum_{\alpha \in \mathcal{A}} N_I^\alpha \, c^\alpha. \tag{2.19}$$

It is now necessary to determine what FE equations the electric potential should satisfy. Standard FE practice is to multiply by the shape functions and integrate by parts, a procedure which produces:

$$\int_\Omega \nabla N_I \cdot \nabla \phi \, \mathrm{d}V = \frac{1}{\epsilon_0} \int_\Omega N_I q \, \mathrm{d}V - \int_\Gamma N_I \mathbf{E} \cdot n \, \mathrm{d}S. \tag{2.20}$$

Here, the electric field is given by $\mathbf{E} = -\nabla \phi$ and must be prescribed on boundaries with a free potential. If the FE electric potential is an expansion in the shape functions,

$$\hat{\phi}(\mathbf{x}) = \sum_I N_I(\mathbf{x}) \phi_I, \tag{2.21}$$

and the continuous charge density is approximated by the FE projection eq. (2.19), the FE equation for the potential is

$$\sum_J \int_\Omega \nabla N_I \cdot \nabla N_J \phi_J \, \mathrm{d}V = \frac{1}{\epsilon_0} \sum_J \int_\Omega N_I N_J q_J \, \mathrm{d}V - \int_\Gamma N_I \mathbf{E} \cdot n \, \mathrm{d}S. \tag{2.22}$$

In contrast to the AtC projection, continuous integrals are retained because all quantities involved are continuous. This difference highlights the contrast between intrinsic (atomic-based) and extrinsic (non-atomic-based) fields.

## 2.2.2 Atomic Electric Field

While the equations discussed in the previous subsection describe the FE component of the electrical interaction, capturing interactions at scales finer than the grid is important to accurately represent the dynamics of charged particles in proximity. Tractability implies that a finite cutoff distance is needed, as is standard in MD. Outside of this cutoff, the only information regarding charge information between two particles is provided by the large scale electric field. However, inside this cutoff radius the interaction is most accurately described by the Coulombic interaction. Denote the set of atoms within the cutoff radius of atom $\alpha$ as $\mathcal{N}_\alpha$, then the total electrostatic force on atom $i$ is:

$$\mathbf{f}_e^\alpha = \sum_{\beta \in \mathcal{N}_\alpha} h(\mathbf{x}^\alpha, \mathbf{x}^\beta) \frac{kc^\alpha c^\beta}{r_{\alpha\beta}^2} \mathbf{r}'_{\alpha\beta} - c^\alpha \nabla \hat{\phi}^*(\mathbf{x}^\alpha) - c^\alpha \sum_{\beta \in \mathcal{N}_\alpha} \left[1 - h(\mathbf{x}^\alpha, \mathbf{x}^\beta)\right] \nabla \hat{\phi}^\beta(\mathbf{x}^\alpha), \qquad (2.23)$$

where $\mathbf{r}'_{\alpha\beta}$ is the unit vector in the direction of $\mathbf{r}_{\alpha\beta} = \mathbf{x}_\beta - \mathbf{x}_\alpha$ and $\hat{\phi}^*$ denotes the electric potential induced by all atoms in the set $\mathcal{A}\backslash\mathcal{N}_\alpha$ and the FE boundary conditions. In contrast, $\hat{\phi}^\beta$ accounts only for the FE potential generated by atoms within the cutoff radius of atom $\alpha$. The force has been decomposed into a Coulombic and FE short-range force, which can be smoothly varied between the two by adjusting the function $h$. Many MD potentials (e.g., CHARRM [10]) include such smoothing. While it will be taken to be unity throughout this work, none of the further development depends on the functional form of $h$ so anisotropic and inhomogeneous smoothing of the electric field is possible within this framework. Because the potential satisfies a linear equation, eq. (2.23) can be rewritten as

$$\mathbf{f}_e^\alpha = \sum_{\beta \in \mathcal{N}_\alpha} h(\mathbf{x}^\alpha, \mathbf{x}^\beta) \frac{kc^\alpha c^\beta}{r_{\alpha\beta}^2} \mathbf{r}'_{\alpha\beta} - c^\alpha \nabla \hat{\phi}(\mathbf{x}^\alpha) + c^\alpha \sum_{\beta \in \mathcal{N}_\alpha} h(\mathbf{x}^\alpha, \mathbf{x}^\beta) \nabla \hat{\phi}^\beta(\mathbf{x}^\alpha). \qquad (2.24)$$

Given the expression for the total electrostatic force acting on atom $\alpha$ in eq. (2.24), the Coulombic interaction is computed from the MD while the large-scale electric field is applied directly from the FE. It therefore remains to determine an effective manner in which to compute the contribution of the electric field at an atom strictly from its neighbors. Directly solving for the electric potential based on this set is a burdensome cost because it must be repeated over every atom and scales with the cost of the FE mesh. Instead, a method using Green's functions computed on the FE mesh is preferable. The Green's function associated with the $I^{th}$ node satisfies the system of equations:

$$\sum_K \int_\Omega \nabla N_J \cdot \nabla N_K G_K^I \, dV = \frac{1}{\epsilon_0} \delta_{I,J}. \qquad (2.25)$$

13

with $\delta_{I,J}$ being the Kronecker delta, which in this case is unity for the $K^{th}$ equation and zero for all others. Boundary conditions are taken to be homogeneous by definition in eq. (2.25). The factor of $1/\epsilon_0$, while not necessary, is retained to facilitate later notation. The nodal variables $G_J^I$ define the response of each mesh node, $J$, to an impulse at the $I^{th}$ node. A solution for the total potential at every node $I$ can be written as

$$\phi_I = \sum_J f_J G_I^J - \int_\Gamma N_I \mathbf{E} \cdot n \, \mathrm{d}S, \tag{2.26}$$

where

$$f_I = \sum_J \int_\Omega N_I N_J q_J \, \mathrm{d}V. \tag{2.27}$$

Using this formulation, the potential due to only the neighbors is defined by two operations:

$$\sum_{\gamma \in \mathcal{A}} N_I^\gamma \sum_J N_J^\gamma q_J^\beta \Delta V^\gamma = N_I^\beta c^\beta, \quad \forall \beta \in \mathcal{N}_\alpha, \tag{2.28}$$

$$\phi_I^\beta = \sum_J \left( \sum_K \int_\Omega N_J N_K q_K^\beta \, \mathrm{d}V \right) G_I^J. \tag{2.29}$$

This framework allows the potential at atom $\alpha$ due to its neighbors to be easily evaluated. However, eq. (2.28) requires solution for a set of nodal variables for each atom while eq. (2.29) necessitates evaluating integrals over the entire FE domain and storing a nodal field for every atom. Also, a nodal field for every node is required to store all the Green's functions. Therefore, while this approach successfully eliminates the solution of the FE electric potential per atom, there is still a need to introduce a series of approximations to reduce its computational and storage expense.

The cost of this method, in terms of both CPU and memory, is associated with the global nature of the FE quantities for both the restricted charge density and the Green's functions. Specifically, the projection in eq. (2.28) generates a charge density field that will in general have non-zero nodal values for all nodes in the mesh. Similarly, evaluating the integral in eq. (2.29) requires data at every node in the mesh because the shape functions can be non-local and the Green's function will be non-zero everywhere. A way to mitigate this expense is to use "localized" projection operators that limit the effect of the atomic quantities on the nodal variables in eq. (2.28) to a bounded domain. One means of producing such operators is by approximating the mass matrices using row-sum lumping, changing the projection eq. (2.6) to:

$$\sum_\alpha N_I^\alpha q_I \Delta V^\alpha = \sum_\alpha N_I^\alpha c^\alpha. \tag{2.30}$$

If this approximation is consistently applied to the right-hand side of eq. (2.22), in conjunction with eq. (2.10), the governing equation for the FE potential becomes

$$\sum_J \int_\Omega \nabla N_I \cdot \nabla N_J \phi_J \, \mathrm{d}V = \frac{1}{\epsilon_0} \sum_\alpha N_I^\alpha c^\alpha + \int_\Gamma N_I \mathbf{E} \cdot n \, \mathrm{d}S. \tag{2.31}$$

---
**Algorithm 1** Determination of Green's Function Sparsity Pattern
---
 1: color all nodes red
 2: insert node $I$ to list SPARSITY
 3: color node $I$ black
 4: list NEIGHBORS = set of all nodes sharing shape function support with node $I$
 5: insert all nodes in NEIGHBORS in SPARSITY
 6: color nodes in NEIGHBORS black
 7: enqueue nodes in NEIGHBORS in queue NEXT-NODES
 8: **while** NEXT-NODES is not empty **do**
 9:   pop NEXT-NODES to node $J$
10:   list NEXT-NEIGHBORS = set of all red nodes sharing shape function support with node $J$
11:   insert all nodes in NEXT-NEIGHBORS in SPARSITY
12:   color all nodes in list NEXT-NEIGHBORS black
13:   **if** node $J$ is within the cutoff radius of any node in NEIGHBORS **then**
14:     enqueue all nodes in NEXT-NEIGHBORS in NEXT-NODES
15:   **end if**
16: **end while**
---

This immediately reduces eq. (2.29) to

$$\phi_I^\beta = \sum_J N_J^\beta c^\beta G_I^J \tag{2.32}$$

through the use of eq. (2.10). Note that without row-sum lumping, all the Green's functions would have to be retained due to quadrature errors in eq. (2.10).

The operation count for computing the short-range FE field using eq. (2.32) scales as $O(n^\alpha n^\beta)$ ($n^\alpha$ is the number of atoms, $n^\beta$ is the average number of neighbors per atom) because $n^\beta$ sums must be performed per atom. This is the same operation count as is needed to evaluate the Coulombic interactions, and naturally fits into the domain decomposition mode of parallelism. However, the factor contained in the scaling itself depends on the number of FE nodes because each term in the sum involves a vector of data at each node. If a large grid is used, the cost of evaluating the short-range FE electric forces will dominate the short-range Coulombic force computation.

The situation can be remedied by storing each $G^I$ sparsely, which is reasonable because only those atoms which are neighbors will have this short-range interaction. The nodal truncation can be computed *a priori* along with the Green's functions by using Algorithm 1 to compute the lists of retained nodes. This algorithm guarantees that all nodes with shape functions corresponding to atom pairs that could be neighbors if one of them is in the support of node $I$ are included, but no others are. If the mesh size is bounded below, then the number of nodes retained in each sparsity pattern is bounded above and independent of the total number of nodes in a mesh. This allows the short-range interactions to be correctly accounted for in an efficient manner.

## 2.3 Boundary Condition Models

Imposing classical boundary conditions on MD systems presents a challenge because, at the scales of MD, boundary conditions are actually fluctuating quantities rather than fixed constraints. This section describes how some can be applied. The first boundary conditions considered are Neumann conditions, which involve the normal derivatives that appear explicitly in eq. (2.17). If the system is immersed in a strong and known electric field, setting **E** at the boundaries to this quantity will impose the correct conditions. It can also be based on known currents because these are proportional to the electric field strength. If far field data indicate there is no overall electric field or current, this quantity should be set to zero because that is correct on average.

The next case of interest is a charged infinite surface, which will occur in an MD calculation if one or two dimensions parallel to the surface are periodic. Because an infinite surface carries infinite charge, a potential cannot be assigned to this surface. Rather, a bulk electric field should be applied perpendicular to the surface with strength based on the desired surface charge. At the surface, the potential is set to zero so that the total electric potential is the sum of the charge that sets up the bulk electric field with the potential induced by the charged particles represented in the MD.

In addition to the surface charge, special considerations must be given to the periodic boundaries. Within the current implementation the potential is not computed in Fourier space and therefore cannot be determined to a constant. Instead, a single (arbitrary) node must be fixed to an arbitrary value. A prerequisite for this approach is the net charge within the simulation box is zero or the spatially varying component of the potential due to point charges is no longer periodic. Further complications are created through the Green's function equation, eq. (2.25). The Green's function of interest in this case is non-periodic and infinite because the short-range charges should affect only interacting pairs rather than the infinite number of interactions of an atom with all the periodic images of its neighbors. Overcoming this challenge is possible; for example the infinite Green's function can be approximated on a larger mesh or the analytic Green's function projected onto the existing basis. However, such an effort is beyond the scope of this work. Instead the PPPM method is used to account for the electric forces in those directions while the AtC approach only applies forces in the non-periodic directions even though the electric potential is three-dimensional. A small error is introduced using this approach because the vertical component will have a slight overcorrection due to the presence of its periodic images.

A final case of interest is the inclusion of a finite, fixed potential surface. In this work, a fixed potential surface is a surface with a given charge distribution with the potential set to the self-induced value everywhere on the surface. A surface with a fixed charge will have a varying potential due to the presence of external charge sources, such as point charges. In large systems, it is reasonable to assume that an external voltage will maintain a potential roughly constant in time, but at the small time and length scales present in MD, this is an approximation. The surface charge would also depend on the electronic properties of the surface. For example, the surface charge in a conductor will vary to maintain no electric field

inside the conducting body, while other surfaces would require a more complex relationship between surface charge and voltage. These effects are not included in the surface charge model that follows, but are somewhat mitigated by the inclusion of short-range interactions with the wall.

Consider a fixed charged on a finite surface specified on a set of FE faces that must not be periodic in any direction. Because the faces are finite, a constant surface charge density will not maintain a constant potential. The potential due to a continuous charge $\sigma(\mathbf{x})$ on a surface can be determined by:

$$V(\mathbf{x}) = \int_S \frac{k\sigma(\mathbf{s})}{\|\mathbf{x} - \mathbf{s}\|} \, \mathrm{d}S. \tag{2.33}$$

The FE projection for the voltage is:

$$\sum_{J \in \mathcal{S}} \int_S N_I N_J V_J \, \mathrm{d}S = \int_S N_I V(\mathbf{s}) \, \mathrm{d}S = \int_S N_I \left( \int_{S'} \frac{k\sigma(\mathbf{s}')}{\|\mathbf{s} - \mathbf{s}'\|} \, \mathrm{d}S' \right) \mathrm{d}S, \quad \forall I \in \mathcal{S}, \tag{2.34}$$

where $\mathcal{S}$ is the set of FE nodes belonging to surface $S$. The integral on the right-hand side of eq. (2.34) can be evaluated using standard FE face quadrature. As an aside, if the charge distribution is also defined by an FE expansion, eq. (2.34) becomes

$$\sum_{J \in \mathcal{S}} \int_S N_I N_J V_J \, \mathrm{d}S = \sum_{J \in \mathcal{S}} \int_S N_I \left( \int_{S'} \frac{k N_J \sigma_J}{\|\mathbf{s} - \mathbf{s}'\|} \, \mathrm{d}S' \right) \mathrm{d}S, \quad \forall I \in \mathcal{S}. \tag{2.35}$$

Equation (2.35) defines a linear relationship between the nodal potential on a surface and its associated nodal charge. The nodal charge for a fixed potential can be determined by solving for $\sigma_J$ after setting each nodal charge to be fixed.

Within the multiscale framework for the electric potential, the surface charge will play a similar role to the atomic charges in that they both induce a long-range potential and provide short-range interactions. To consider these types of interactions, we further expand eq. (2.24) by accounting for the surface charge in the electric potential

$$\mathbf{f}_e^\alpha = \sum_{\beta \in \mathcal{N}_\alpha} h(\mathbf{x}^\alpha, \mathbf{x}^\beta) \frac{k c^\alpha c^\beta}{r_{\alpha\beta}^2} \mathbf{r}'_{\alpha\beta} + c^\alpha \sum_I \int_{S \bigcap B(\mathbf{x}^\alpha, r_c)} h^s(\mathbf{x}^\alpha, \mathbf{s}) \frac{k N_I \sigma_I}{\|\mathbf{x}^\alpha - \mathbf{s}\|^2} \mathbf{r}'_{\alpha s} \, \mathrm{d}S$$

$$- c^\alpha \nabla \phi^\alpha + + c^\alpha \sum_{\beta \in \mathcal{N}_\alpha} h(\mathbf{x}^\alpha, \mathbf{x}^\beta) \nabla \hat{\phi}^\beta(\mathbf{x}^\alpha) + c^\alpha \int_{S \bigcap B(\mathbf{x}^\alpha, r_c)} h^s(\mathbf{x}^\alpha, \mathbf{s}) \nabla \hat{\phi}_s^\alpha \, \mathrm{d}S. \tag{2.36}$$

The first integral accounts for the exact short-range force exerted by the surface charge while the second integral is a correction removing the effect of the surface charge through the FE potential on atom $\alpha$. Both integrals can be evaluated directly using FE quadrature, although other quadrature schemes (e.g., based on atoms contained in those faces) would be possible. The potential induced by the surface charge can be determined by computing Green's functions for each of the quadrature points by first solving eq. (2.35) for the induced surface potential of a unit charge and then solving the the electric potential equation treating the surface as a fixed potential boundary.

In general, these Green's function are highly non-local because charge at any point on a surface induces a non-zero potential everywhere on the surface, as shown in eq. (2.35). However, the resulting short-range interactions can still be localized by truncating the Green's functions to only those nodes within a cutoff radius of the surface. As in the case with the potential induced by charged particles, the Green's functions can be computed and stored during a pre-computation phase. This method is a low-storage, low-cost approach that accounts for accurate short- and long-range interactions between charged MD atoms and prescribed surface data. An important point to note is that for a given quadrature scheme to evaluate the surface integrals in eq. (2.36), each quadrature point will require its own Green's function.

## 2.4   Implementation Details

The methods described above were implemented in LAMMPS within an existing AtC framework. This framework generates a FE overlaying a region of atoms and computes piecewise linear shape function values and derivatives at FE quadrature points and atomic locations. A pre-processing step first computes the nodal neighbor list for each node based on the force cutoff radius according to Algorithm 1. Then the stiffness matrix is set up for the electric potential, eq. (2.31), and used to compute each Green's function according to eq. (2.25). Green's functions are then truncated and stored in sparse vectors based on the nodal neighbor lists. At the same time, fixed potential boundary values are determined by eq. (2.34). Then the Green's function for each surface quadrature point used to evaluate eq. (2.34) is calculated by solving eq. (2.31).

The bulk of the work of this method occurs immediately after the LAMMPS force calculation step, which is between the two steps in the Verlet integration scheme. At each time step the shape function matrices used in the projection operation (eq. (2.6)) must be updated to the new positions of the atoms. After this is done, the matrices in the FE atomic volume equation are known.

After the shape function-related quantities are updated, the charges can be restricted using eq. (2.19) with row-sum lumping to form the right-hand side for the FE electric potential, eq. (2.31), enabling its calculation using the pre-computed stiffness matrix. Neumann conditions are applied by adjusting the right-hand side during the solve while Dirichlet conditions are satisfied by a penalty method. This method weights the diagonal entry of all fixed nodes with a value $10^4$ greater relative to the maximum diagonal value in the left-hand-side matrix. Correspondingly, the right-hand side is modified by adding the same penalty factor multiplying the desired potential value.

LAMMPS adds in the Coulombic interaction before the present method is executed, so only the last two terms in eq. (2.24) need to be accounted for. The first, accounting for the total FE electric field, is added to all atoms. Afterwards, the truncated FE potential associated with each atom is computed using the Green's functions multiplied by the restricted

atomic charges. This preprocessing step allows the neighbor FE potentials for each atom to be quickly calculated by summing over the FE potential contribution of all its neighbors. The potential is then corrected to result in the appropriate electric force at each atom using eq. (2.24).

Charged surfaces are implemented in an approximate manner. In a pre-processing step, consistent with a form of row-sum lumping approximation of eq. (2.34), the potential is determined from a fixed charge by

$$V_I = \sum_W \frac{k\sigma(w)}{|x_I - w|} W, \tag{2.37}$$

where $W$ denotes the Gauss quadrature points and weights on the face. This approach ensures the denominator is always non-zero. To evaluate the short-range interactions, the nodes are used as effective charge locations with charge set to the shape-function weighted integral of the surface charge,

$$\sigma_I = \int_\Gamma N_I \sigma(\mathbf{x}) \, \mathrm{d}S, \tag{2.38}$$

with the integral evaluated using the same Gaussian quadrature as eq. (2.37).

When computing the short-range surface interactions and corrections in eq. (2.36) only nodes within the cutoff radius of each atom are considered, and then their Green's functions are used to remove the FE potential. As a simplifying approximation, face-specific Green's functions are not computed for the charge at each quadrature point that contributes to the charge at node $I$ in eq. (2.38). Instead, only their contributions to the potential at node $I$ are considered, which allows the same Green's functions as those used in eq. (2.32) to be reused. The net effect of all these approximations are that low-order integration is used to evaluate the first integral in eq. (2.36) while the correction from the second integral does not take into account all the long-range impact of local charge on the fixed potential boundary condition applied in eq. (2.31). Improvements can be made by improving the order of integration over the surface within the cutoff radius and more accurately estimating the impact of charge associated with quadrature points on the electric potential. A final improvement in performance can be realized by maintaining neighbor lists at each surface quadrature point to avoid the search over all atoms to determine those near a wall (walls are currently implemented in LAMMPS with this more expensive approach as well). These improvements in the implementation of charged surfaces, as well as more general models for other types of surfaces and periodic boundary corrections for eq. (2.24) are deferred for future work.

This page intentionally left blank.

# Chapter 3

# Computational Results

## 3.1  Basic Verification Test Case

To verify the basic correctness and implementation of the method, a simple stack of atoms was set up with periodic conditions along the span $(y, z)$. Periodic conditions on the atomic forces were also used along the length of the stack $(x)$ to maintain the equilibrium structure. A FCC lattice structure with spacing $4.08\,\text{Å}$, resulting in 144 atoms, was used to develop a test case amenable to analytical solution. Around this lattice a FE mesh was constructed to represent the continuous charge distributions and electric field. While the elements have non-zero volume, periodicity in the $y$ and $z$ directions effectively makes the elements one dimensional with length $2.04\,\text{Å}$. However the FE mesh is not periodic in the $x$ direction so fixed potential and electric field boundary conditions can be applied. The overall structure is shown in Fig. 3.1(a).

The electric field in this case was driven by both boundary conditions and internal charges. Each atom was given a unit charge (equivalent of a proton) such that the system's charge density was uniform at $5.89 \times 10^{-2}$ unit charges per $\text{Å}^3$. The FE potential was fixed to zero at the left end. At the right end, either an insulating or fixed electric field condition was used. The known boundary conditions and charge densities allow the analytic solution to Poisson's equation to be determined. As shown in Fig. 3.1, in both cases the analytic solution is recovered by the method. This case tests the Poisson solver, projection operations, and computation of the atomic volume. The results verify their implementation and demonstrate that the overall mathematical formulation of the problem is reasonable given the behavior of the FE system.

## 3.2  Comparison with Existing Methods: PPPM and Ewald Sums

Providing a quantitative comparison of the present method with existing approaches for including long-range electrostatic forces in MD is an important aspect of verifying the technique. These are primarily PPPM and Ewald sums as described in Chapter 1. Because they are only appropriate for periodic systems, a fully periodic FCC lattice system is created with
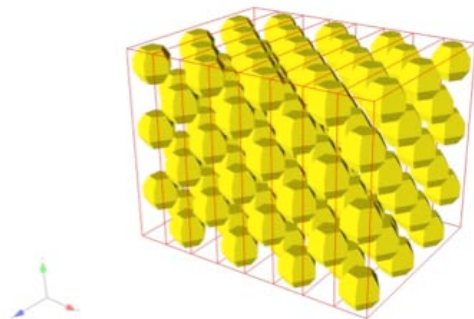
(a) Basic Verification Case Schematic
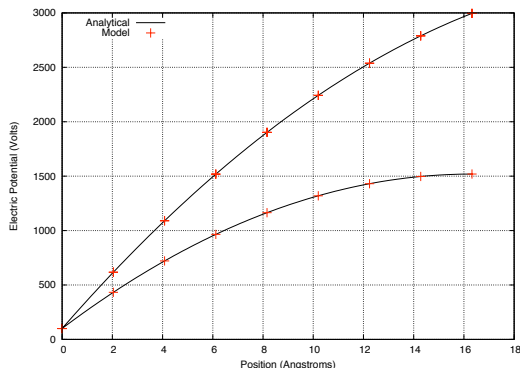


(b) Basic Verification Case Results

**Figure 3.1.** Basic verification test case. Figure 3.1(a) shows the problem set up while 3.1(b) presents the results for different boundary conditions.

dimensions $65.28 \times 12.24 \times 12.24$ Å and lattice spacing of $4.08$ Å, corresponding to 576 atoms. The atoms are uncharged except for a group with a positive unit charge and a group with a negative unit charge, as shown in Fig. 3.2 (note this is the finest FE mesh). Initial computations were performed with the short-range Coulombic force disabled so that the only forces acting on the atoms are the long-range forces generated by the method. As shown in Table 3.1, the method produces forces similar to the other methods. In each case the force acting on the negatively charged atoms is presented because the net force was zero for all methods. To see how this is related to the FE fields, Fig. 3.3 shows the FE charge density and electric potential variables. The charge density is simply the approximate projection of the atomic state and enters into the right-hand side of the equation governing the electric potential. On the coarsest mesh, inadequate resolution exists to accurately solve the gradients needed in this equation, resulting in error in the solution.

This test demonstrates the correctness of the theory and implementation regarding the prolongation of the long-range force from the FE to the atoms, including the use of FE shape functions to take derivatives of the electric potential. It further demonstrates that the method is comparably accurate to existing methods, even though the finest FE grid had only 256 elements while the automatically generated PPPM method required a grid of $320 \times 90 \times 90$ Fourier collocation points to achieve an error of $10^{-4}$. This is the only case considered in this work in which a fully periodic system is considered because dynamics were not evaluated, and therefore the short-range FE correction was not needed (recall the current correction scheme is inappropriate in periodic directions). However, to use the FE method the node corresponding to $x = y = z = 0$ was fixed to have zero potential so the Poisson equation would be well posed. These modifications enabled a quantitative comparison with existing methods that use periodic boundaries.
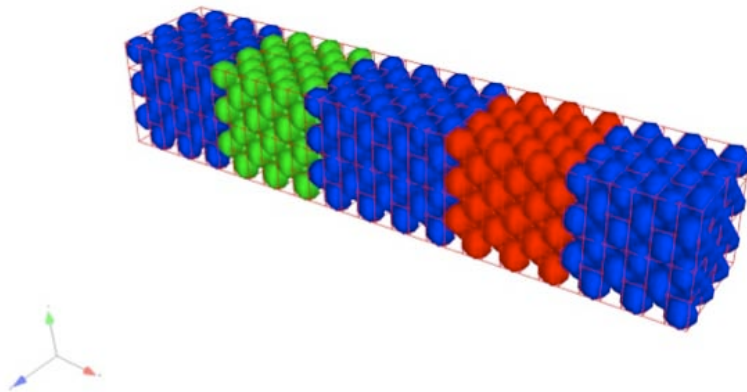
**Figure 3.2.** Schematic of the PPPM and Ewald comparison case with the present method. Red atoms are positively charged, green atoms are negatively charged, and blue atoms are neutral.

## 3.3 Comparison with Full Anisotropic Solution

There is one other technique to incorporate long-range electrical interactions between charged particles in MD: "brute force" calculation of the electric field using a finite MD simulation with a Coulombic cutoff distance greater than the maximum possible atomic separation. Such an approach is impractical for most simulations because the cost of building the neighbor lists and computing the interatomic electrical interactions is prohibitive. It is also inappropriate for periodic systems because an infinite cutoff radius would be required.

The model system built to examine this case consists of an FCC gold lattice with spacing $4.08\,\text{Å}$ over a horizontal span of $22.44 \times 22.44\,\text{Å}^2$. The lattice is not periodic in any direction,

**Table 3.1.** Comparison of the force computed by the long-range electric field. The present method, with entries denoted by the mesh size, is shown along with existing approaches.

| Force $\left(\frac{\text{g ps}}{\text{Å}^2\ \text{mol}}\right)$ | Method/Mesh |
|---|---|
| $8.49533 \times 10^6$ | PPPM |
| $8.49543 \times 10^6$ | Ewald sums |
| $4.71971 \times 10^6$ | $8 \times 1 \times 1$ elements |
| $8.49547 \times 10^6$ | $16 \times 1 \times 1$ elements |
| $8.49547 \times 10^6$ | $32 \times 1 \times 1$ elements |
| $8.49547 \times 10^6$ | $32 \times 2 \times 2$ elements |
| $8.49547 \times 10^6$ | $32 \times 4 \times 4$ elements |

(a) Finite Element Charge Density
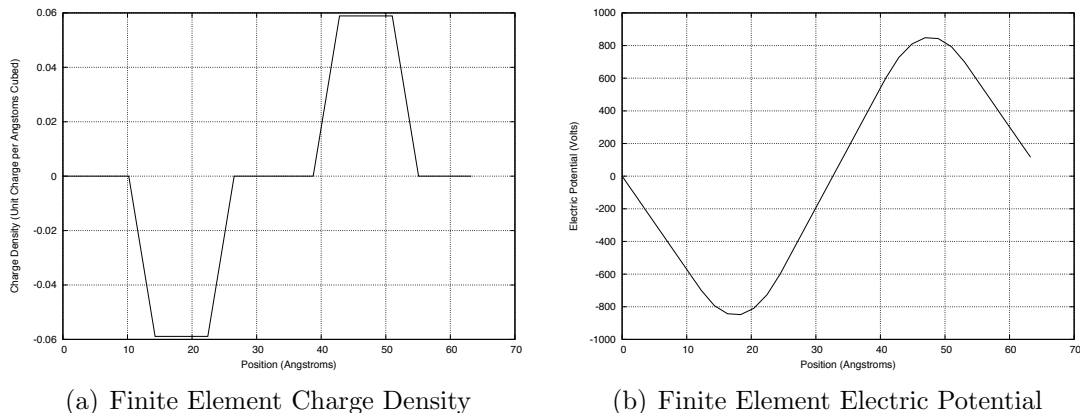


(b) Finite Element Electric Potential

**Figure 3.3.** Finite element fields from the finest mesh used to compare against the PPPM method and Ewald Sums. Figure 3.3(a) shows charge density and 3.3(b) presents the electric potential using this charge density as a source.

so three layers of gold atoms at the bottom and along the sides are held fixed to stabilize the lattice, which has a depth of 12.24 Å. Because the spatial symmetry is broken, the resulting lattice must be minimized to determine its equilibrium configuration. Liquid argon is then added on top of this structure to a height of 22.44 Å, with the total dimensions of the box selected as the maximum size such that the neighbor lists could fit in the available memory and still be long enough for atoms at opposite ends of the box to be neighbors. The liquid argon was allowed to equilibrate for 50 ps with a time step of 0.5 fs using the NVT ensemble. A schematic of the system, including the FE mesh, is shown after the equilibration step in Fig. 3.4. Upon creation, certain argon atoms were randomly chosen to have a positive unit charge so that during equilibration they tend to separate. These atoms are bounded by applying 9-3 Leonard-Jones walls along the five sides without gold to serve as a wall. All inter-atomic forces were modeled using Leonard-Jones interactions. Gold-gold interactions use $\epsilon = 0.724$ eV and $\sigma = 2.598$ Å, while the argon-argon model has $\epsilon = 0.010$ eV and $\sigma = 3.405$ Å. A uniform cutoff radius of 13.0 Å localizes the interactions, and cross-species interactions use parameters mixed with the arithmetic rule.

After the system has come to a statistical steady state, the top layer of gold atoms is negatively charged with an amount so that it can be effectively screened by the ions. This case loosely corresponds to the electric double layer commonly observed on charged surfaces in aqueous solutions. This configuration is run to a steady state using only Coulombic interactions with a long cutoff distance of 40 Å as well as the proposed method using a much more modest distance of 13 Å. Exactly resolving all long Coulombic interactions was the limiting factor in choosing this geometry. The FE mesh was created over the liquid using $4^3$ uniform elements of size approximately 175 Å$^3$. When using the AtC method the gold atom charge was removed in favor of a fixed-charge boundary and its corresponding spatially varying potential. Zero electric field (Neumann) boundary conditions were used on
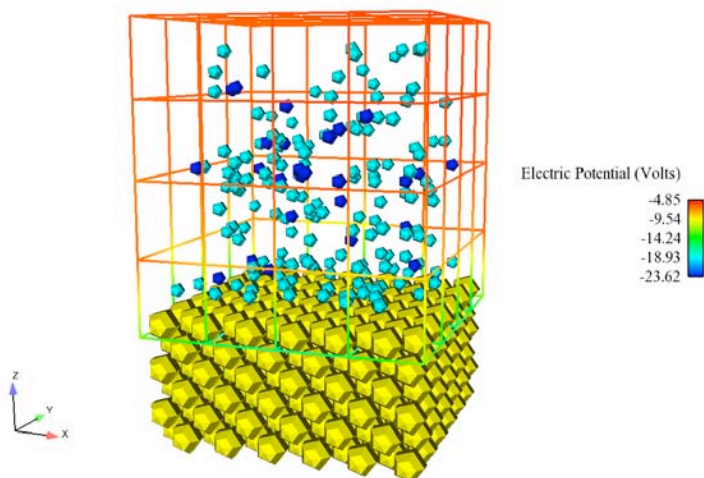
**Figure 3.4.** Schematic of the fully anisotropic configuration. Gold atoms are yellow, neutral argon atoms are light blue, and positively charged argon atoms are dark blue. Particles are kept in the box using fictitious 9-3 Leonard-Jones walls at each unbounded side of the mesh, which is colored using the electric potential.

all other sides. This case illustrates the difficulty in exactly translating continuous boundary conditions to an atomistic setting. An insulating condition is only appropriate in the limit of an infinitely small screening layer such that the electric field is zero outside of the domain of interest. This limit is violated even in the steady state of this solution, and is clearly incorrect during the transient. Further, the charged surface is treated as a fixed potential surface by the FE electric potential, when in reality the potential varies based on the distribution of the atoms. In a true conductor, for example, the potential and surface charge would change to make the electric field in the conductor zero. Improved boundary conditions to better account for these physics are beyond the scope of this work.

Despite the inconsistency in between the continuous boundary conditions and the full MD solution can be compared against the MD solution using the long-range FE electric field. An electric potential is computed directly based on the positions and charges of each atom for the MD. Figure 3.5 compares this exact electric potential with that of the electric potential AtC from the AtC calculation at the steady state along a vertical slice of the domain(the mean value of each has been removed). Both the structure and magnitude of the AtC potential compares well with that from the MD simulation. The cause of this good agreement can be ascertained by examining the end states from each of the two methods. In the MD case, all 27 charged atoms lie in an immobile layer near the wall while in the AtC method results in 25 atoms in this layer (based on the particles' trajectories, one of the free atoms is partially screened). By congregating near the wall, these atoms screen the electric field so it drastically reduces in magnitude away from the wall. The dynamics of

these atoms indicate they are highly attracted to the charged wall as they experience only a vibrational motion after their adsorption. Therefore, despite the approximate nature of the insulating FE boundary conditions and the low-order quadrature used to implement the charged surface, good agreement is obtained with the exact solution when using this method in both quantitative and qualitative senses.
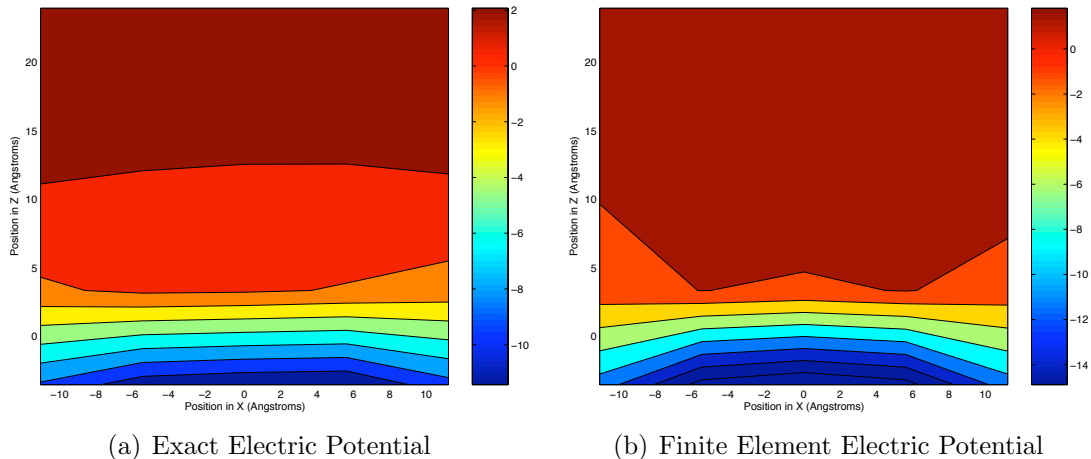


(a) Exact Electric Potential



(b) Finite Element Electric Potential

**Figure 3.5.** Contour plot of the electric potential computed directly from summations over charged particles (3.5(a)) and from the AtC method (3.5(b)). The $X$ axis is parallel to the wall while the $Z$ axis is perpendicular. Units are Volts. The mean value of the potential was removed in both cases.

## 3.4  Electrolyte Flow in a Silicon Nano-Channel

In this case, flow in a nanofluidic device is considered. A full analysis of this configuration is beyond the scope of this work, but the case illustrates how to perform these types of technologically relevant simulations. Silicon crystals form walls at the top and bottom of a region of salt water, which is free to flow in the wall-parallel directions. Periodic conditions are used to allow this flow while the channel walls break the symmetry. Figure 3.7 illustrates the computational geometry. The silicon planes are initialized in a similar manner to the gold in section 3.3 except for the periodic boundaries in the transverse direction. The silicon is arranged in a diamond lattice with the 111 face towards the water, and then the arrangement is adjusted to minimize the potential energy to account for the exposed face. A box of water containing sodium and and chlorine ions is initialized for 1 ns in a fixed region using the NVT ensemble and 9-3 Leonard-Jones walls to contain the fluid in the wall-normal directions. The water is modeled using the TIP3 [8] set of Leonard-Jones coefficients and charges (see Appendix A for more details). After equilibration, the water is inserted between the silicon planes and allowed to readjust for 1 ns. During this phase, the water was integrated using the

(a) Final State Using long-range Interactions

(b) Final State Using AtC Method

**Figure 3.6.** Comparison of the final MD state from the direct calculation (3.6(a)) and the AtC method (3.6(b)). See Fig. 3.4 for the color legend.

NVE ensemble while the silicon followed the NVT ensemble so it could thermally regulate the salt water.

After the entire system comes into equilibrium, electric fields of strength $-10^{-5}$ V/Å were applied in the $x$ (wall-parallel) and $z$ (wall-normal) directions. With these fields in place, ions are forced to flow along the channel in opposite directions as well as aggregate to opposite sides of the channel, resulting in shear flow in the channel. The wall-normal component of the electric field is applied to the atoms using the AtC method while the PPPM approach provides the correct long-range electric forces in the periodic directions. This case was originally considered in [13] using a different methodology to account for the ionic electric field by applying a wall-normal correction to the Ewald summations used to compute the long-range electrostatic interactions in the periodic directions [18]. An electric double layer forms on each surface, which screens the interior ions from the component of the electric field perpendicular to the wall. Hence, the flow is slower near the channel center as it is primarily driven by the ions in the double layers near the walls. This case demonstrates the steps that must be taken to perform these simulations by incrementally building and equilibrating the various components, such as silicon and water, followed by applying separate models for the isotropic and anisotropic components of the electric field.

## 3.5    Nanotube-Layered Electrode

The final MD simulation performed consists of a carpet of carbon nanotubes (CNTs) on a gold electrode. Each tube is anchored to the gold and forms a pore through which ions and water can reach the surface. While much simplified, this geometry serves a surrogate for the types of physics which will be present in the SEI layer. Each CNT has a chirality of (9,0) and length of approximately 20 Å. The transverse dimensions of $41 \times 53.27$ Å$^2$ were chosen such
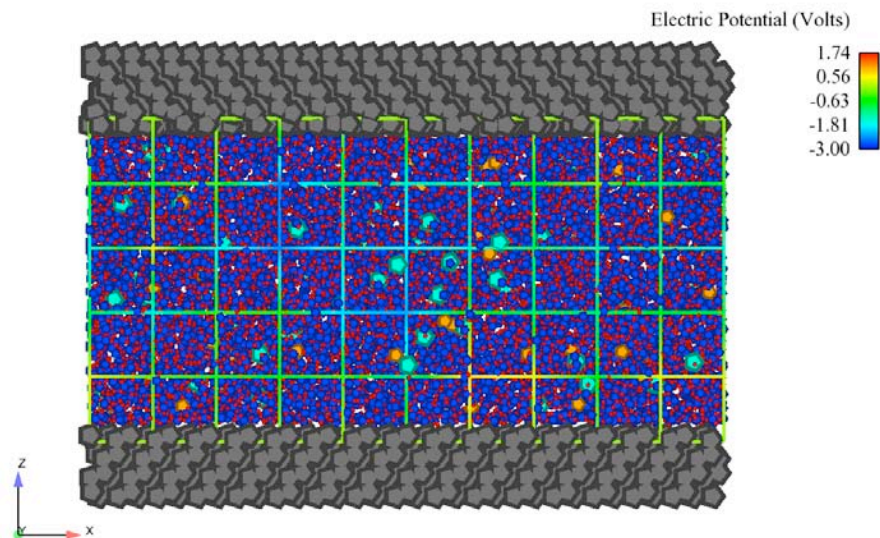
**Figure 3.7.** Schematic of the silicon nanochannel simulation. Water is modeled using hydrogen atoms (red) bonded to oxygen atoms (blue). Other atoms are sodium ions (orange), chlorine ions (light blue), and silicon (grey). The FE mesh is overlaid and colored by the electric potential.

that an integer number of tubes would fit along the wall. Doing so induced a small amount of stress in the gold, which was realized during the minimization phase. The water, containing potassium and chorine ions, was equilibrated separately using the same procedure as in the previous section. To account for the infinite charge on the electrode's surface, an electric field of $-10^{-5}$ V/Å was applied in the normal direction. Periodic boundary conditions were used in the transverse direction and PPPM method applied the long-range electric forces in these directions while the AtC method computed the wall-normal forces. A schematic of the setup is shown in Fig. 3.8.

The analogous dynamics to the SEI layer are the transport of aqueous species through the CNTs to the gold surface. A closer view of this process is provided in Fig. 3.9. Water is able to fill the tubes, but does so in chains similar to previously reported results from isotropic MD simulations [20]. Some potassium ions are able to penetrate through the CNTs, although the water interferes with their transport to the wall. Several ions are observed just above the CNTs that cannot propagate downward due to this effect. In the SEI layer the pores are sufficiently small that the solvent cannot penetrate through it, eliminating one source of resistance to ion transport. This simulation illustrates that the method is appropriate for the general class of dynamics in the SEI layer in terms of applying the necessary anisotropic electric field in a system with transport through porous media.

28
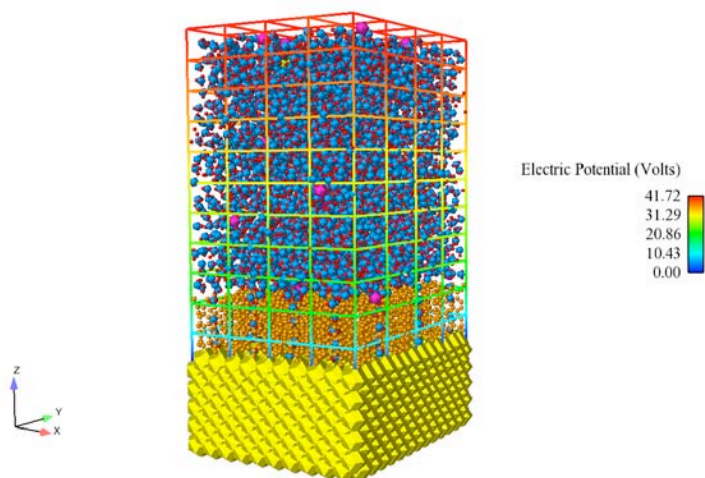
**Figure 3.8.** Schematic of the saltwater, electrode, and CNT simulation. Water is modeled using hydrogen atoms (red) bonded to oxygen atoms (blue). Other atoms are potassium ions (purple), chlorine ions (green), carbon (orange), and gold (yellow). The FE mesh is overlaid and colored by the electric potential.
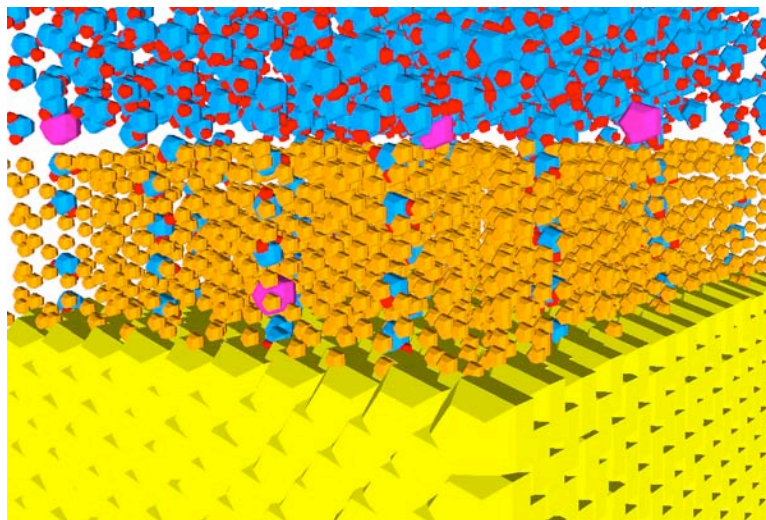


**Figure 3.9.** A close view of ions and water filling the CNTs. See Fig 3.8 for the color legend.

This page intentionally left blank.

# Chapter 4

# Conclusions and Future Work

This work describes a method to apply consistent anisotropic electric fields, including prescribed boundary conditions, to molecular dynamics simulations. By using AtC coupling, the electric potential can be solved on a FE mesh using source terms arising from the atomistic charge distribution. The approach is a significant improvement over current schemes for incorporating long-range electrical interactions, which are restricted to periodic domains. By breaking this symmetry, the AtC electric field enables simulations of more technologically relevant configurations with applied electric fields or potential surfaces.

For the purposes of this effort, the target application are batteries, specifically, understanding the SEI layer in common battery types. This layer plays a strong role in determining battery performance and safety, but is difficult to model with current approaches because of the anisotropy induced by the electrode. However, the electric field must be incorporated to simulate charge transport through the SEI layer. Full simulation of the layer will also require several additional modeling advances.

The first additional set of models that needs to be developed for SEI layer simulation are descriptions for the chemical reactions that occur at the anode. Two primary types of reaction occur. As the SEI layer forms, ions react at the electrode with the electrolyte to form the variety of solid phases that comprise the SEI layer. After its formation, charge transport reactions take place through the layer between ions and the electrode. Adding chemistry models that account for these reactions is an important step. MD offers the opportunity to model binary reactions if the activation energy is known. Because MD explicitly represents all the atomic interactions, interacting pairs of reactants can be identified. Sub- and super-MD scale information is necessary to estimate the probability of a reaction occurring, thereby completing the reaction model. Sub-MD scale information can be determined by theory, experiment, or quantum calculations, and accounts for the impact the collision angle and quantum state have on the probability of a reaction. Super-MD scale data, such as electric field strength, also can alter this probability and can be explicitly modeled within the AtC framework. Implementing such a model will further enhance the ability of MD to represent the SEI layer.

The second model required for full SEI layer models is to incorporate the far field state into the model of the interphase layer. AtC coupling provides a reasonable framework in which to realize this kind of model. The most significant difference between it and previous AtC efforts is that transport is now mediated through atomic motion so new methods must

be developed that can add and remove atoms in accordance with the bulk concentration and velocities. New approaches to managing MD atomic data structures will be required to correctly account for atomic transport in this approach. This is beneficial because solid-fluid interfaces could be directly simulated in MD to accurately represent behavior within a larger device.

While the target application for the method is the SEI layer, its development was performed in a general manner to facilitate future investigations of other types of physics. A logical application would be the electric double layer that forms out of an ionic solution on top of charged or polarizable surfaces. This phenomenon is found in many situations, including EESDs and biological flows. Improved understanding of its performance would have significant technological applications in these areas. Additional areas of interest are flows in porous media where ions are driven by electric fields. A technology that could benefit from a model of this configuration is desalination where nano-structured devices can filter out salt. Beyond these examples, many instances of nano-scale physics influenced by electric fields and charged surfaces have scientific or technological interest, including nano-electromechanical systems (NEMS) and fuel cells. This method provides the ability to break the spatial symmetry in the current simulation techniques and to expand the scope of scientific investigations and engineering applications at the nanoscale.

# References

[1] D.W. Brenner, O.A. Shenderova, J.A. Harrison, S.J. Stuart, B. Ni, and S.B. Sinnott. A second-generation reactive empirical bond order (REBO) potential energy expression for hydrocarbons. *Journal of Physics: Condensed Matter*, 14(4):783–802, 2002.

[2] S. Chowdhuri and A. Chandra. Molecular dynamics simulations of aqeuous NaCl and KCl solutions: effects of ion concentration on the single-particle, pair, and collective dynamical properties of ions and water molecules. *Journal of Chemical Physics*, 115(8):3732–3741, 2001.

[3] M.S. Daw and M.I. Baskes. Embedded-atom method - derivation and application to impurities, surfaces, and other defects in metals. *Physical Review B*, 29(12):6443–6453, 1984.

[4] J.B. Goodenough *et al.* Basic research needs for electrical energy storage. Technical report, Report of the Basic Energy Sciences Workshop for Electrical Energy Storage, April 2007.

[5] S.M. Foiles, M.I. Baskes, and M.S. Daw. Embedded-atom-method functions for the FCC metals Cu, Ag, Au, Ni, Pd, Pt, and their alloys. *Physical Review B*, 33(12):7983–7991, 1986.

[6] R.W. Hockney and J.W. Eastwood. *Computer Simulation using Particles*. Taylor & Francis Group, 1988.

[7] R.E. Jones, J.A. Templeton, G.J. Wagner, D. Olmstead, and N. Modine. Electron-transport enhanced molecular dynamics for metals and semi-metals. *Submitted to the International Journal for Numerical Methods in Engineering*, 2009.

[8] W.L. Jorgensen, J. Chandrasekhar, J.D. Madura, R.W. Impey, and M.L. Klein. Comparison of simple potential functions for simulating liquid water. *Journal of Chemical Physics*, 79(2):926–935, 1983.

[9] S.-P. Ju. A molecular dynamics simulation of the adsorption of water molecules surrounding an Au nanoparticle. *Journal of Chemical Phyics*, 122(9):94718–94723, 2005.

[10] A.D. MacKerell, D. Bashford, M. Bellott, R.L. Dunbrack, J.D. Evanseck, M.J. Field, S. Fischer, J. Gao, H. Guo, S. Ha, D. Joseph-McCarthy, L. Kuchnir, K. Kuczera, F.T.K. Lau, C. Mattos, S. Michnick, T. Ngo, D.T. Nguyen, B. Prodhom, W.E. Reiher, B. Roux, M. Schlenkrich, J.C. Smith, R. Stote, J. Straub, M. Watanabe, J. Wiokiewicz-Kuczera, D. Yin, and M. Karplus. All-atom empirical potential for molecular modeling and dynamics studies of proteins. *Journal of Physical Chemistry B*, 102(18):3586–3616, 1998.

[11] S.J. Plimpton. Fast parallel algorithms for short-range molecular dynamics. *Journal of Computational Physics*, 117:1–19, 1995.

[12] E.L. Pollock and J. Glosli. Comments on P(3)M, FMM, and the Ewald method for large periodic coulombic systems. *Computer Physics Communications*, 95(2-3):93–110, 1996.

[13] R. Qiao and N.R. Aluru. Ion concentrations and velocity profiles in nanochannel electroosmotic flows. *Journal of Chemical Physics*, 118(10), 2003.

[14] Q. Shao, J. Zhou, L. Lu, X. Lu, Y. Zhu, and S. Jiang. Anomalous hydration shell order of $Na^+$ and $K^+$ inside carbon nanotubes. *Nano Letters*, 9(3):989–994, 2009.

[15] F.H. Stillinger and T.A. Weber. Computer-simulation of local order in condensed phases of silicon. *Physical Review B*, 31(8):5262–5271, 1985.

[16] S.J. Stuart, A.B. Tutein, and J.A. Harrison. A reactive potential for hydrocarbons with intermolecular interactions. *Journal of Chemical Phyics*, 112(14):6472–6486, 2000.

[17] G.J. Wagner, R.E. Jones, J.A. Templeton, and M.L. Parks. An atomistic-to-continuum coupling method for heat transfer in solids. *Computational Methods in Applied Mechanics and Engineering*, 197:3351–3365, 2008.

[18] I.-C. Yeh and M.L. Berkowitz. Ewald summation for systems with slab geometry. *Journal of Chemical Physics*, 111:3155, 1999.

[19] B. Yoon, W.D. Luedtke, J. Gao, and U. Landman. Diffusion of gold clusters on defective graphite surfaces. *Journal of Physical Chemistry B*, 107:5882–5891, 2003.

[20] U. Zimmerli, P.G. Gonnet, J.H. Walther, and P. Koumoutsakos. Curvature induced *L*-defects in water conduction in carbon nanotubes. *Nano Letters*, 5(6):1017–1022, 2005.

[21] J.A. Zimmerman, R.E. Jones, and J.A. Templeton. A material frame approach for evaluating continuum variables in atomistic simulations. *Submitted to the Journal of Computational Physics*, 2009.

# Appendix A

# Interatomic Potentials

Tables A.1 and A.2 give the potential type, coefficients, and source for each pair of interactions considered in the simulations. All short-range charged interactions were modeled using Coulombic interactions with a sharp cutoff at $10\,\text{Å}$. References refer to relevant simulations that used these parameters in similar physics to their uses here, except for the Stillinger-Weber (SW), embedded atom method (EAM), and AIREBO potentials in which references are provided to a presentation describing their source. Parameters for Leonard-Jones (LJ) interactions are the energy depth of the well $\epsilon$, the length scale $\sigma$, and the cutoff radius $r_c$. For the Morse potential the parameters are the energy $D_0$, inverse length scale $\alpha$, equilibrium distance $r_0$, and cutoff radius $r_0$. The units used are Angstroms for length and and electron Volts for energy. For the more complex potentials, references are given to their parameter sets used in this application. Note that hydrogen atoms only interact with other atoms electrically and had no other interatomic potential. The only exception are the hydrogens in nanotubes, which interacted with carbon atoms in the nanotubes, as indicated in the $C/H - C/H$ entry in Table A.1. When multiple references are provided, it implies the Leonard-Jones parameters were mixed using the arithmetic rule. Finally, differences between interactions common to both types of simulations were chosen to match [13] in the case of the silicon nano-channel.

**Table A.1.** Interaction potential, potential coefficients, and reference for pairwise interactions in gold simulations.

| Atom 1 | Atom 2 | Potential | Coefficients | Source |
|--------|--------|-----------|--------------|--------|
| O | O | LJ | $\epsilon = 0.006596$, $\sigma = 3.1507$, $r_c = 10$ | [8] |
| O | K | LJ | $\epsilon = 0.005348$, $\sigma = 3.24085$, $r_c = 10$ | [8, 2] |
| O | Cl | LJ | $\epsilon = 0.005348$, $\sigma = 3.77535$, $r_c = 10$ | [8, 2] |
| O | C | LJ | $\epsilon = 0.004475$, $\sigma = 3.35035$, $r_c = 10$ | [8, 14] |
| O | Au | Morse | $D_0 = 0.0668$, $\alpha = 1.3$, $r_0 = 3.7$, $r_c = 9$ | [9] |
| K | K | LJ | $\epsilon = 0.004336$, $\sigma = 3.331$, $r_c = 10$ | [2] |
| K | Cl | LJ | $\epsilon = 0.004336$, $\sigma = 3.8655$, $r_c = 10$ | [2] |
| K | C | LJ | $\epsilon = 0.003629$, $\sigma = 3.4405$, $r_c = 10$ | [2, 14] |
| K | Au | LJ | $\epsilon = 0.0056043$, $\sigma = 2.9645$, $r_c = 10$ | [2, 21] |
| Cl | Cl | LJ | $\epsilon = 0.004336$, $\sigma = 4.4$, $r_c = 10$ | [2] |
| Cl | C | LJ | $\epsilon = 0.003629$, $\sigma = 3.975$, $r_c = 10$ | [2, 14] |
| Cl | Au | LJ | $\epsilon = 0.056043$, $\sigma = 3.499$, $r_c = 10$ | [2, 21] |
| C | C | AIREBO | see [16] | [1] |
| C | Au | LJ | $\epsilon = 0.01273$, $\sigma = 2.9943$, $r_c = 10$ | [19] |
| Au | Au | EAM | see [5] | [3] |

**Table A.2.** Interaction potential, potential coefficients, and reference for pairwise interactions in silicon simulations.

| Atom 1 | Atom 2 | Potential | Coefficients | Source |
|--------|--------|-----------|--------------|--------|
| O | O | LJ | $\epsilon = 0.006740$, $\sigma = 3.1650$, $r_c = 10$ | [13] |
| O | Na | LJ | $\epsilon = 0.005348$, $\sigma = 3.24085$, $r_c = 10$ | [13] |
| O | Cl | LJ | $\epsilon = 0.005348$, $\sigma = 3.77535$, $r_c = 10$ | [13] |
| O | Si | Morse | $D_0 = 0.0668$, $\alpha = 1.3$, $r_0 = 3.7$, $r_c = 9$ | [13] |
| K | K | LJ | $\epsilon = 0.004336$, $\sigma = 3.331$, $r_c = 10$ | [13] |
| K | Cl | LJ | $\epsilon = 0.004336$, $\sigma = 3.8655$, $r_c = 10$ | [13] |
| Na | Na | LJ | $\epsilon = 0.004336$, $\sigma = 3.331$, $r_c = 10$ | [13] |
| Na | Cl | LJ | $\epsilon = 0.004336$, $\sigma = 3.8655$, $r_c = 10$ | [13] |
| Na | Si | LJ | $\epsilon = 0.0056043$, $\sigma = 2.9645$, $r_c = 10$ | [13] |
| Cl | Cl | LJ | $\epsilon = 0.004336$, $\sigma = 4.4$, $r_c = 10$ | [13] |
| Cl | Si | LJ | $\epsilon = 0.056043$, $\sigma = 3.499$, $r_c = 10$ | [13] |
| Si | Si | SW | see [15] | [15] |

# DISTRIBUTION:

5   Jonathan Lee
    Mailbox 106
    Rice University
    Dept. of Mechanical Engineering & Materials Science - MS 321
    PO Box 1892
    Houston TX 77251-1892

| | | |
|---|---|---|
| 1 | MS 1322 | John Aidun, 1435 (electronic) |
| 1 | MS 1322 | Richard Muller, 1435 (electronic) |
| 1 | MS 0836 | Terrence Aselage, 1514 (electronic) |
| 1 | MS 9001 | Chris Moen, 8000 (electronic) |
| 1 | MS 9042 | Michael Chiesa, 8246 (electronic) |
| 5 | MS 9404 | Reese Jones, 8246 |
| 5 | MS 9404 | Jonathan Zimmerman, 8246 |
| 5 | MS 9403 | Bryan Wong, 8223 |
| 1 | MS 9054 | Robert Carling, 8300 (electronic) |
| 1 | MS 9161 | Stewart Griffiths, 8300 (electronic) |
| 1 | MS 9054 | Art Pontau, 8360 (electronic) |
| 1 | MS 9409 | Scott James, 8365 (electronic) |
| 1 | MS 9161 | Robert Nilson, 8365 (electronic) |
| 5 | MS 9409 | Jeremy Templeton, 8365 |
| 1 | MS 9409 | Gregory Wagner, 8365 (electronic) |
| 1 | MS 9291 | Anup Singh, 8621 (electronic) |
| 1 | MS 9161 | Sarah Allendorf, 8656 (electronic) |
| 2 | MS 9018 | Central Technical Files, 8944 |
| 1 | MS 0899 | Technical Library, 8944 (electronic) |
| 1 | MS 0123 | D. Chavez, LDRD Office, 1011 |

This page intentionally left blank.